Table 1
Previously reported missense mutations in *HSPG2* in SJS.

Position (hg19/GRCh37)	Exon	cDNA	Amino acid	Domain	Reference
chr1: 22202483G>A	24	c.3056C>T	p.Pro1019Leu	III-2	[4,17]
chr1: 22191530G>A	36	c.4432C>T	p.Arg1478Cys	III-3	[4]
chr1: 22191367C>T	36	c.4595G>A	p.Cys1532Tyr	III-3	[2]
chr1: 22190685G>A	37	c.4648C>T	p.Arg1550Cys	III-3	[4]
chr1: 22162131C>T	75	c.10355G>A	p.Arg3452Gln	IV	[4]
chr1: 22159874C>T	80	c.10982G>A	p.Arg3661Gln	IV	[4]

Genomic coordinates are according to hg19/GRCh37. cDNA positions are according to NM_005529.5.

inside the cells. A similar study with a similar result has been reported for p.Cys1532Tyr in domain III-3 [21]. Rodgers and colleagues initially reported that p.Cys1532Tyr-knockin mice did not exhibit typical features of SJS [21]. Nicole and colleagues, however, later reported that the p.Cys1532Tyr-knockin mice exhibited partial deficiency of endplate acetylcholinesterase [12], dysmyelination of the preterminal Schwann cells [11], and continuous neuromyotonic discharges [10]. Among the seven missense mutations including the currently reported one in *HSPG2* causing SJS, five are clustered in domain III (Fig. 1). Domain III has been known to bind to and regulate growth factors including FGF7 [22,23], FGF18 [24], and PDGF [25]. As both the p.Leu1088Pro and p.Cys1532Tyr mutations similarly inhibit secretion of perlecan, domain III is also likely to be crucial for secreting perlecan into the extracellular space.

Acknowledgements

This study was supported by Grants-in-Aid from the MEXT and MHLW of Japan.

Appendix: Supplementary material

Supplementary data to this article can be found online at doi:10.1016/j.nmd.2015.05.002.

References

[1] Schwartz O, Jampel RS. Congenital blepharophimosis associated with a unique generalized myopathy. Arch Ophthalmol 1962;68:52–7.
[2] Nicole S, Davoine CS, Topaloglu H, et al. Perlecan, the major proteoglycan of basement membranes, is altered in patients with Schwartz-Jampel syndrome (chondrodystrophic myotonia). Nat Genet 2000;26:480–3.
[3] Arikawa-Hirasawa E, Le AH, Nishino I, et al. Structural and functional mutations of the perlecan gene cause Schwartz-Jampel syndrome, with myotonic myopathy and chondrodysplasia. Am J Hum Genet 2002;70:1368–75.
[4] Stum M, Davoine CS, Vicart S, et al. Spectrum of HSPG2 (perlecan) mutations in patients with Schwartz-Jampel syndrome. Hum Mutat 2006;27:1082–91.
[5] Arikawa-Hirasawa E, Wilcox WR, Le AH, et al. Dyssegmental dysplasia, Silverman-Handmaker type, is caused by functional null mutations of the perlecan gene. Nat Genet 2001;27:431–4.
[6] Rieubland C, Jacquemont S, Mittaz L, et al. Phenotypic and molecular characterization of a novel case of dyssegmental dysplasia, Silverman-Handmaker type. Eur J Med Genet 2010;53:294–8.
[7] Arikawa-Hirasawa E, Watanabe H, Takami H, Hassell JR, Yamada Y. Perlecan is essential for cartilage and cephalic development. Nat Genet 1999;23:354–8.
[8] Costell M, Gustafsson E, Aszodi A, et al. Perlecan maintains the integrity of cartilage and some basement membranes. J Cell Biol 1999;147:1109–22.
[9] Whitelock JM, Melrose J, Iozzo RV. Diverse cell signaling events modulated by perlecan. Biochemistry 2008;47:11174–83.
[10] Echaniz-Laguna A, Rene F, Marcel C, et al. Electrophysiological studies in a mouse model of Schwartz-Jampel syndrome demonstrate muscle fiber hyperactivity of peripheral nerve origin. Muscle Nerve 2009;40:55–61.
[11] Bangratz M, Sarrazin N, Devaux J, et al. A mouse model of Schwartz-Jampel syndrome reveals myelinating Schwann cell dysfunction with persistent axonal depolarization in vitro and distal peripheral nerve hyperexcitability when perlecan is lacking. Am J Pathol 2012;180:2040–55.
[12] Stum M, Girard E, Bangratz M, et al. Evidence of a dosage effect and a physiological endplate acetylcholinesterase deficiency in the first mouse models mimicking Schwartz-Jampel syndrome neuromyotonia. Hum Mol Genet 2008;17:3166–79.
[13] Peng HB, Xie H, Rossi SG, Rotundo RL. Acetylcholinesterase clustering at the neuromuscular junction involves perlecan and dystroglycan. J Cell Biol 1999;145:911–21.
[14] Ito M, Suzuki Y, Okada T, et al. Protein-anchoring strategy for delivering acetylcholinesterase to the neuromuscular junction. Mol Ther 2012; 20:1384–92.
[15] Li H, Durbin R. Fast and accurate long-read alignment with Burrows-Wheeler transform. Bioinformatics 2010;26:589–95.
[16] Koboldt DC, Zhang Q, Larson DE, et al. VarScan 2: somatic mutation and copy number alteration discovery in cancer by exome sequencing. Genome Res 2012;22:568–76.
[17] Bell CJ, Dinwiddie DL, Miller NA, et al. Carrier testing for severe childhood recessive diseases by next-generation sequencing. Sci Transl Med 2011;3:65ra4.
[18] Bauche S, Boerio D, Davoine CS, et al. Peripheral nerve hyperexcitability with preterminal nerve and neuromuscular junction remodeling is a hallmark of Schwartz-Jampel syndrome. Neuromuscul Disord 2013; 23:998–1009.
[19] Arikawa-Hirasawa E, Rossi SG, Rotundo RL, Yamada Y. Absence of acetylcholinesterase at the neuromuscular junctions of perlecan-null mice. Nat Neurosci 2002;5:119–23.
[20] Vorechovsky I. Transposable elements in disease-associated cryptic exons. Hum Genet 2010;127:135–54.
[21] Rodgers KD, Sasaki T, Aszodi A, Jacenko O. Reduced perlecan in mice results in chondrodysplasia resembling Schwartz-Jampel syndrome. Hum Mol Genet 2007;16:515–28.
[22] Ghiselli G, Eichstetter I, Iozzo RV. A role for the perlecan protein core in the activation of the keratinocyte growth factor receptor. Biochem J 2001;359:153–63.
[23] Sher I, Zisman-Rozen S, Eliahu L, et al. Targeting perlecan in human keratinocytes reveals novel roles for perlecan in epidermal formation. J Biol Chem 2006;281:5178–87.
[24] Smith SM, West LA, Hassell JR. The core protein of growth plate perlecan binds FGF-18 and alters its mitogenic effect on chondrocytes. Arch Biochem Biophys 2007;468:244–51.
[25] Whitelock JM, Iozzo RV. Heparan sulfate: a complex polymer charged with biological activity. Chem Rev 2005;105:2745–64.

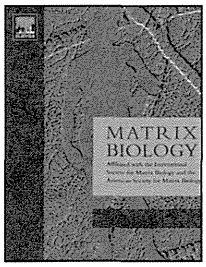

Perlecan inhibits autophagy to maintain muscle homeostasis in mouse soleus muscle

Liang Ning[a], Zhuo Xu[a,1], Norihiko Furuya[b,c], Risa Nonaka[a], Yoshihiko Yamada[d] and Eri Arikawa-Hirasawa[a,b]

***a* - Research Institute for Diseases of Old Age,** *Juntendo University Graduate School of Medicine, Tokyo 113-8421, Japan*
***b* - Department of Neurology,** *Juntendo University Graduate School of Medicine, Tokyo 113-8421, Japan*
***c* - Department of Neuroscience for Neurodegenerative Disorders,** *Juntendo University Graduate School of Medicine, Bunkyo-ku, Tokyo 113-8421, Japan*
***d* - National Institute of Dental and Craniofacial Research,** *NIH, Bethesda 90814, USA*

Correspondence to Eri Arikawa-Hirasawa: *at: Juntendo University Faculty of Medicine, Research Institute for Diseases of Old Age, Building 10, Room 606, 2-1-1 Hongo, Bunkyo-ku, Tokyo 113-8421, Japan. ehirasaw@juntendo.ac.jp*
http://dx.doi.org/10.1016/j.matbio.2015.08.002

Abstract

The autophagy–lysosome system is essential for muscle protein synthesis and degradation equilibrium, and its dysfunction has been linked to various muscle disorders. It has been reported that a diverse collection of extracellular matrix constituents, including decorin, collagen VI, laminin α2, endorepellin, and endostatin, can modulate autophagic signaling pathways. However, the association between autophagy and perlecan in muscle homeostasis remains unclear. The mechanical unloading of perlecan-deficient soleus muscles resulted in significantly decreased wet weights and cross-section fiber area compared with those of control mice. We found that perlecan deficiency in slow-twitch soleus muscles enhanced autophagic activity. This was accompanied by a decrease in autophagic substrates, such as p62, and an increase in LC3II levels. Furthermore, perlecan deficiency caused a reduction in the phosphorylation levels of p70S6k and Akt and increased the phosphorylation of AMPKα. Our findings suggested that perlecan inhibits the autophagic process through the activation of the mTORC1 pathway. This autophagic response may be a novel target for enhancing the efficacy of skeletal muscle atrophy treatment.

Introduction

Skeletal muscle is a plastic tissue that continuously adapts in response to a variety of stimuli, including use and disuse. Mechanical load causes hypertrophy, while physical inactivity leads to atrophy. Muscle mass is in a dynamic equilibrium between protein synthesis and protein degradation, the latter being ensured by the ubiquitin–proteasome pathway and the autophagy process [1]. Animal models of skeletal muscle atrophy have been used to identify various pathways, including the autophagy–lysosomal pathway, the matrix–metalloproteinase (MMP) pathway, and the ubiquitin–proteasome pathway, via methods such as hindlimb casting, denervation, and Achilles tendon tenotomy. Atrophy induced via tenotomy has been shown to increase the expression of MMP genes and genes involved in the lysosomal degradation pathway [2]. It has also been shown that soleus muscle from autophagy-impaired (Atg7-deficient: Atg7 KO) mice maintained muscle mass, while soleus muscle from wild type mice and fast-twitch muscles from both wild type and Atg7 KO mice atrophied after denervation; this indicated that autophagy contributed to denervation atrophy in the soleus muscle [3].

Perlecan, a heparan sulfate proteoglycan (HSPG), is a component of basement membranes that surrounds the skeletal muscle. Perlecan is implicated in many biological functions in tissue development, homeostasis, and diseases [4–8]. It is also implicated in modulating cellular processes by regulating growth factor signaling pathways [9–12]. We have previously

0022-2836/© 2015 Published by Elsevier B.V.

Please cite this article as: L. Ning, et al., Perlecan inhibits autophagy to maintain muscle homeostasis in mouse soleus muscle, Matrix Biol (2015), http://dx.doi.org/10.1016/j.matbio.2015.08.002

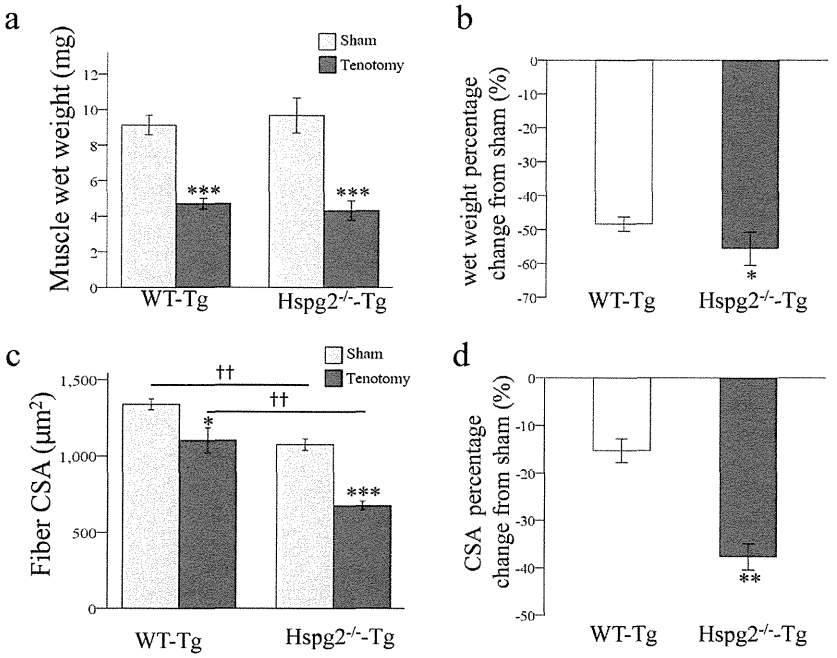

Fig. 1. Tenotomy enhances soleus muscle loss significantly in Hspg2$^{-/-}$Tg mice. (a) Wet weights of soleus muscles. To examine the effect of tenotomy in the soleus muscle, the gastrocnemius and soleus muscles but not the plantaris muscle were tenotomized (G/S-Ten) in the distal tendons of the left hindlimbs, and the wet weight of the soleus muscle was measured 14 days after surgery. Data are shown as the mean ± s.e.m. ***$P < 0.001$ vs. the contralateral sham muscle from the right limb. (b) Percentage change in muscle wet weight. The effect of unloading on muscle wet weight was determined by comparing muscle wet weight to the contralateral sham muscle from the right limb; *$P < 0.05$ vs. WT-Tg mice. (c) Quantification of the cross-sectional area (CSA) of the soleus muscle. Data are shown as the mean ± s.e.m. *$P < 0.05$, ***$P < 0.001$ vs. the contralateral sham muscle from the right limb of the same mice. $^{††}P < 0.01$ vs. WT-Tg mice. (d) Percentage change in muscle CSA. The effect of unloading on muscle CSA was determined by comparing muscle wet weights from the CSA of the contralateral sham muscle from the right limb. Data are shown as the mean ± s.e.m. **$P < 0.001$ vs. WT-Tg mice.

demonstrated that mechanical overload of the plantaris muscle, a fast-twitch skeletal muscle, in perlecan-deficient mice causes greater muscle increase and that mechanical unload causes less muscle loss, accompanied by decreased myostatin expression and signaling [13]. Myostatin is preferentially expressed in fast-twitch fibers, and inactivating mutations are essentially associated with fast-twitch fiber hyperplasia [14]. However, due to the lack of myostatin in the soleus muscle, the differences between the contributions of different signaling pathways to the atrophy of fast-twitch and slow-twitch muscles in perlecan-deficient mice remains to be clarified.

Macroautophagy (simply referred to as autophagy hereafter) is a basic catabolic mechanism that involves the degradation of unnecessary or dysfunctional cellular components through the action of lysosomes [15]. It is regarded as an important process that maintains tissue integrity and overall organismal homeostasis [16–18]. Abnormal autophagy, defined by either inadequate autophagy levels or hyperactive autophagic flux, is detrimental to normal tissue function and manifests as neurological disorders such as Parkinson's disease or congenital myopathies [19]. The alteration of autophagy contributes to myofiber degeneration, which leads to the accumulation of abnormal organelles. Extracellular matrix proteins, such as decorin, collagen VI, laminin α2, endostatin, endorepellin, and kringle V, modulate the autophagic signaling pathway [19]. For example, collagen VI, endorepellin, decorin, kringle V, and endostatin promote autophagy [20], while laminin α2 inhibits the autophagy process [21]. The C-terminal fragment of perlecan, endorepellin, inhibits angiogenesis in vitro and in vivo [22]. More recently, endorepellin has been shown to promote autophagy in endothelial cells by regulating the expression of autophagy marker genes [23].

In this report, we studied the association between perlecan and autophagy in the slow-twitch soleus muscle using a lethality-rescued perlecan knockout

Please cite this article as: L. Ning, et al., Perlecan inhibits autophagy to maintain muscle homeostasis in mouse soleus muscle, Matrix Biol (2015), http://dx.doi.org/10.1016/j.matbio.2015.08.002

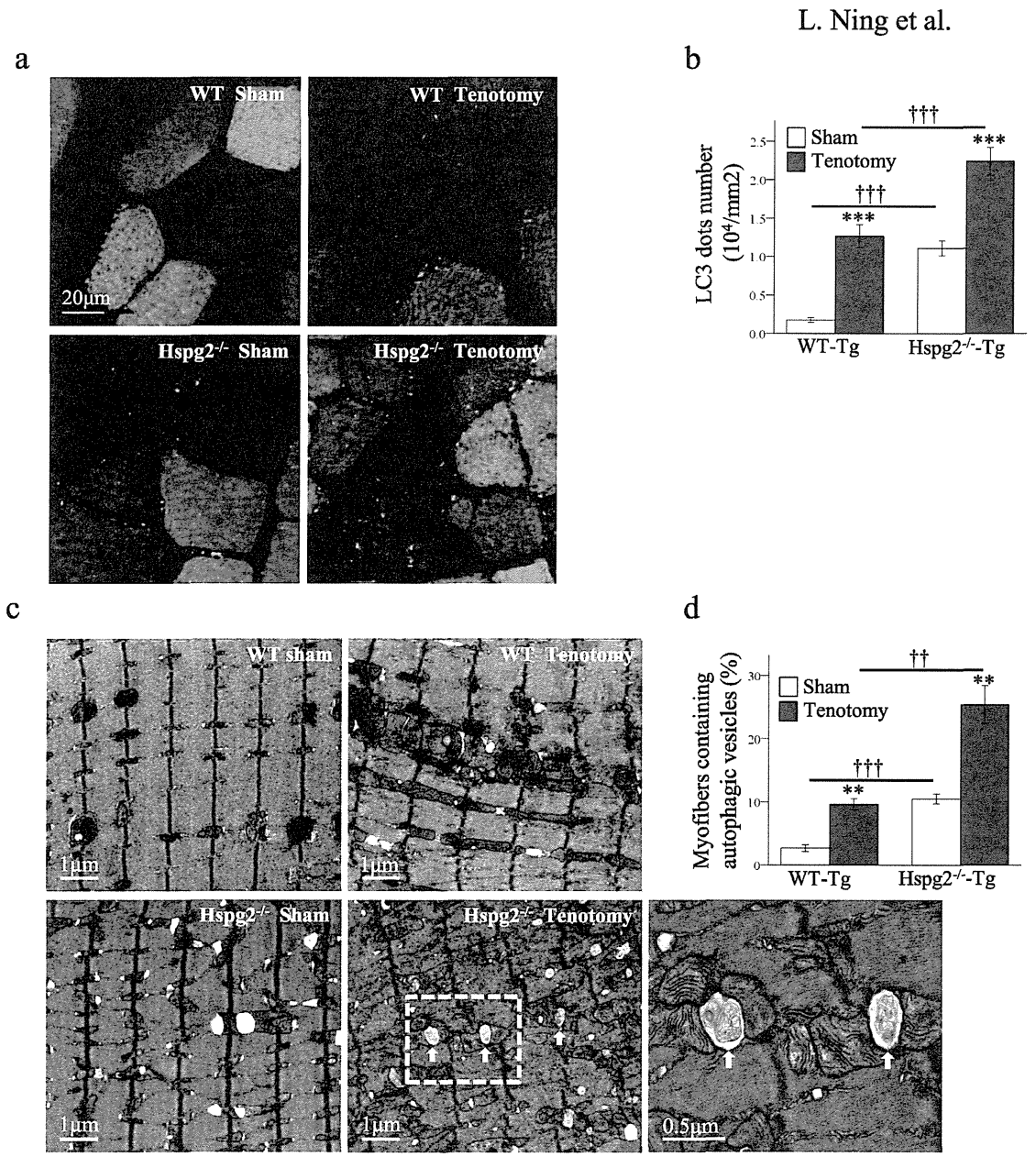

Fig. 2. Autophagy is increased in soleus muscles from Hspg2$^{-/-}$Tg mice. (a) Representative images of the sham and tenotomized soleus muscles from double–transgenic WT-Tg/GFP-LC3-Tg mice and Hspg2$^{-/-}$Tg/GFP-LC3-Tg mice at 14 d after the operation. (b) The number of GFP-LC3 dots was counted and divided by the corresponding area. For the analysis of the skeletal muscles, transverse sections were used. The y-axis indicates the number of GFP-LC3 dots (10^4/mm^2). Each value represents the mean ± s.e.m. ***P < 0.001 vs. Sham, †††P < 0.001 vs. WT-Tg mice. (c) Electron micrographs of the sham and tenotomized soleus muscles from transgenic WT-Tg, Hspg2$^{-/-}$Tg mice at 14 d after the operation. The boxed region in the Hspg2$^{-/-}$ tenotomy panel is shown in the next panel on the right. Arrow: autophagic vacuoles. (d) Percentage of myofibers containing autophagic vesicles in sham and tenotomized soleus of WT-Tg and Hspg2$^{-/-}$Tg mice. Each value represents the mean ± s.e.m. **P < 0.01 vs. Sham, ††P < 0.01, †††P < 0.001 vs. WT-Tg mice.

mouse model (Hspg2$^{-/-}$; Tg), in which the perlecan transgene is expressed specifically in cartilage but not other tissues, including muscles [24]. Our results revealed that perlecan deficiency enhanced autophagy of the slow-twitch soleus muscle through the inhibition of the mTORC1 pathway.

Please cite this article as: L. Ning, et al., Perlecan inhibits autophagy to maintain muscle homeostasis in mouse soleus muscle, Matrix Biol (2015), http://dx.doi.org/10.1016/j.matbio.2015.08.002

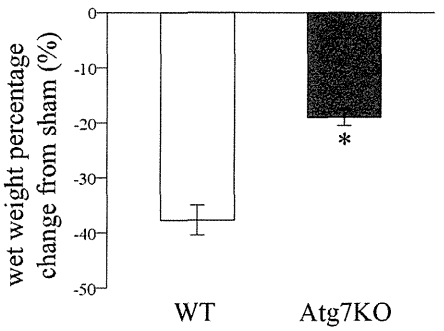

Fig. 3. Percentage change in muscle wet weight of WT mice and Atg7 KO mice. The effect of unloading on muscle wet weight was determined by comparing muscle wet weight to the contralateral sham muscle from the right limb; *P < 0.05 vs. WT mice.

Results

The absence of perlecan increases the level of tenotomy-induced atrophy in the soleus muscle

We first examined the role of perlecan in tenotomy-induced atrophy in the soleus muscle of the perinatal lethality-rescued perlecan knockout ($Hspg2^{-/-}$; Tg) mice, which express the perlecan transgene specifically in cartilage under the control of the Col2a1 collagen promoter and enhancer [25] in $Hspg2^{-/-}$ mice [13]. In the previous study, we showed that perlecan is absent in skeletal muscle, the kidneys, the heart, and the liver in $Hspg2^{-/-}$Tg mice, whereas it is expressed in those tissues in WT-Tg mice, and the recombinant perlecan is expressed in the cartilage of $Hspg2^{-/-}$Tg mice [13].

To analyze the role of perlecan in the mechanical unloading of slow twitch muscles, we performed tenotomy of the distal tendons of the left hindlimbs of WT-Tg and $Hspg2^{-/-}$Tg mice. The soleus and the gastrocnemius muscles were tenotomized, but the plantaris muscle was left intact in both groups of mice (soleus and gastrocnemius tenotomized, G/S-Ten). At 14 days post-surgery, the wet weights of the soleus muscles were compared with those of the non-tenotomized muscles of the right hindlimbs, which underwent a control sham operation. The wet weights of the unloaded soleus muscle in the WT-Tg- and $Hspg2^{-/-}$Tg-G/S-Ten mice were 48% and 56% lower, respectively, than in the sham-operated WT-Tg-Con and $Hspg2^{-/-}$Tg-Con mice (Fig. 1a). In the soleus muscles of $Hspg2^{-/-}$Tg mice, unloading led to a more significant reduction in wet weight ($P < 0.05$) (Fig. 1b). We further measured the cross section area (CSA) of the soleus muscle unloaded via the G/S-Ten operation. The CSAs of the unloaded soleus muscles in the WT-Tg- and $Hspg2^{-/-}$Tg-G/S-Ten mice were 18% and 37% smaller, respectively, than those in the sham-operated WT-Tg-Con and $Hspg2^{-/-}$Tg-Con mice (Fig. 1c). In the soleus muscles of $Hspg2^{-/-}$Tg mice, unloading caused a more significant decrease in CSAs ($P < 0.05$) (Fig. 1d). These results indicate that perlecan deficiency enhanced unloading-induced soleus muscle atrophy.

Perlecan deficiency increases the number of autophagosomes

Autophagy can contribute to muscle loss during atrophy [26] and sarcopenia [27]. To determine whether autophagy contributes to the increased atrophy of $Hspg2^{-/-}$Tg soleus muscles, we first analyzed the number of autophagosomes in perlecan-deficient muscles. We crossed $Hspg2^{-/-}$Tg mice with GFP-LC3 transgenic mice [28], and their progeny underwent a tenotomy operation. We then investigated the number of green fluorescent protein (GFP)-positive puncta, which is representative of autophagosomes, in the WT-Tg and $Hspg2^{-/-}$Tg mice. The number of GFP-LC3 puncta in the soleus muscle was higher in the $Hspg2^{-/-}$Tg mice than in the WT-Tg mice under both the sham and unloading conditions (Fig. 2a and b). We then analyzed the ultrastructure of the soleus muscles of WT-Tg and $Hspg2^{-/-}$Tg mice under sham and tenotomy conditions (Fig. 2c). There were no defects detected in the architecture of the contractile apparatus or in the mitochondria of the WT-Tg-Con muscles. Although the contractile apparatus seemed normal in the WT-Tg-Ten and $Hspg2^{-/-}$Tg-Con mice, we observed degenerating mitochondria and a small number of autophagic vacuoles (AVs). In muscles derived from the $Hspg2^{-/-}$Tg-Ten mice, we observed the more prominent presence of autophagosomes (Fig. 2c and d) associated with degenerating mitochondria.

Mechanical unloading-induced atrophy is prevented in autophagy-deficient soleus muscle

To determine whether autophagy contributes to tenotomy atrophy in the soleus muscle, we used an autophagy deficient mouse model [3].

The mice were generated with a skeletal muscle-specific Atg7 (an essential gene for autophagy) knockout under the control of the tamoxifen-inducible human skeletal actin (HAS) promoter ($Atg7^{Flox/Flox}$: HAS-Cre-ER^{T2}, hereinafter referred to as Atg7 KO mice). The soleus muscles of Atg7 KO mice showed resistance to atrophy at 14 d after tenotomy (Fig. 3), suggesting a direct effect of autophagy deficiency on muscle atrophy. These results indicate that autophagy contributes to tenotomy atrophy.

Please cite this article as: L. Ning, et al., Perlecan inhibits autophagy to maintain muscle homeostasis in mouse soleus muscle, Matrix Biol (2015), http://dx.doi.org/10.1016/j.matbio.2015.08.002

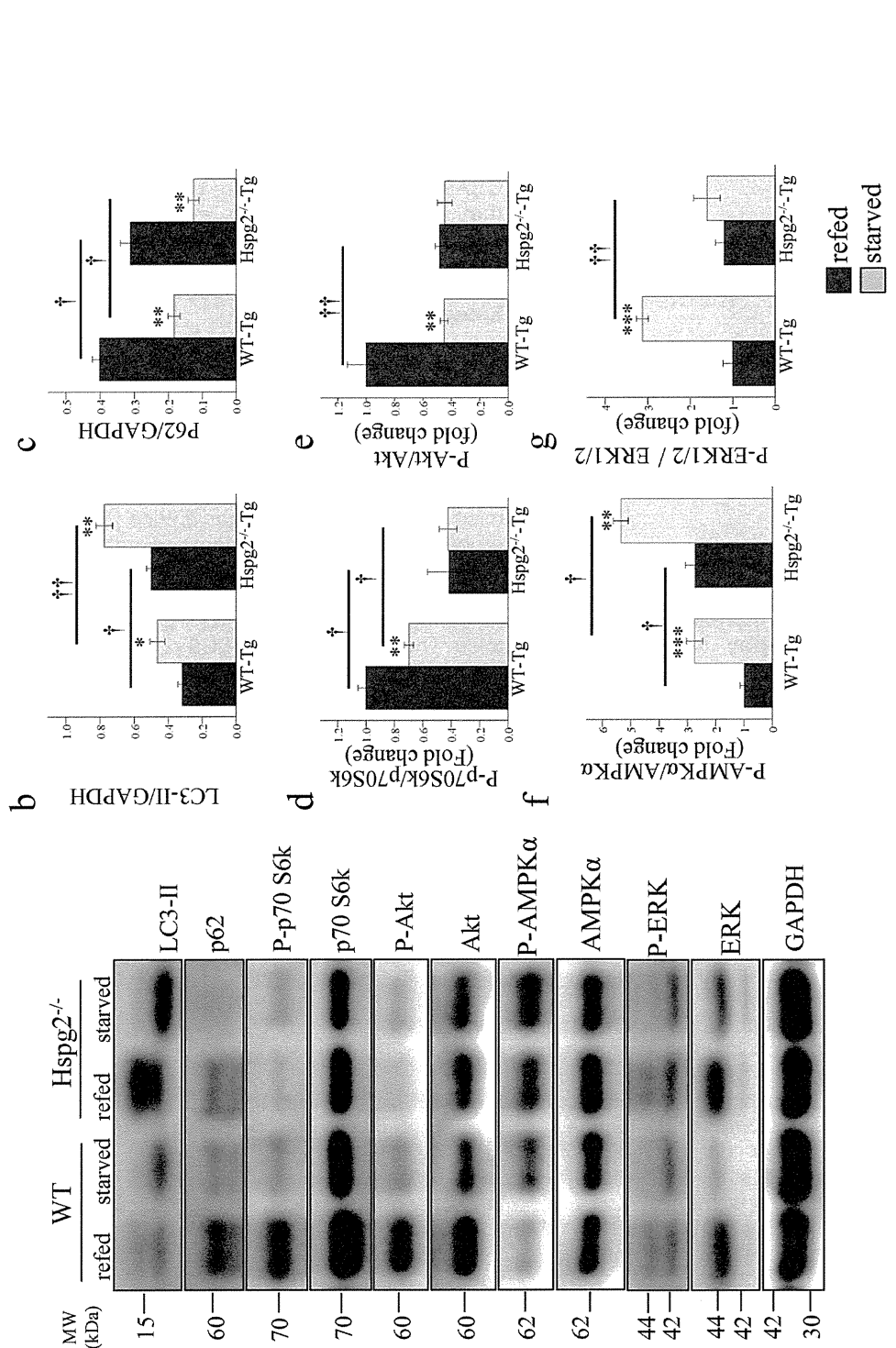

Fig. 4. Autophagy induction and the activity of the Akt/mTORC1 pathway in the soleus muscle from 24-h-fasted WT-Tg and Hspg2$^{-/-}$ Tg mice. (a) Immunoblotting results represent the levels of LC3II, p62, P-p70S6K, P-Akt, P-AMPKα, and P-ERK in the soleus muscles from refed and starved WT-Tg and Hspg2$^{-/-}$Tg mice were determined by Western blot. (b) Densitometric quantification of LC3II and p62 level, normalized against GAPDH. Each value represents the mean ± s.e.m. *P < 0.05; **P < 0.01 vs. refed mice. †P < 0.05, ††P < 0.01 vs. WT-Tg mice. (d, e, f, g) Relative activity, expressed as the ratio of activated phospho-p70S6K to total p70S6K, phospho-Akt to total Akt, phospho-AMPKα to total AMPKα and phospho-ERK to total ERK, was quantified as the fold increase relative to the soleus muscles of the refed WT-Tg mice. Each value represents the mean ± s.e.m. **P < 0.01 vs. refed mice, †P < 0.05, ††P < 0.01 vs. WT-Tg mice.

Please cite this article as: L. Ning, et al., Perlecan inhibits autophagy to maintain muscle homeostasis in mouse soleus muscle, Matrix Biol (2015), http://dx.doi.org/10.1016/j.matbio.2015.08.002

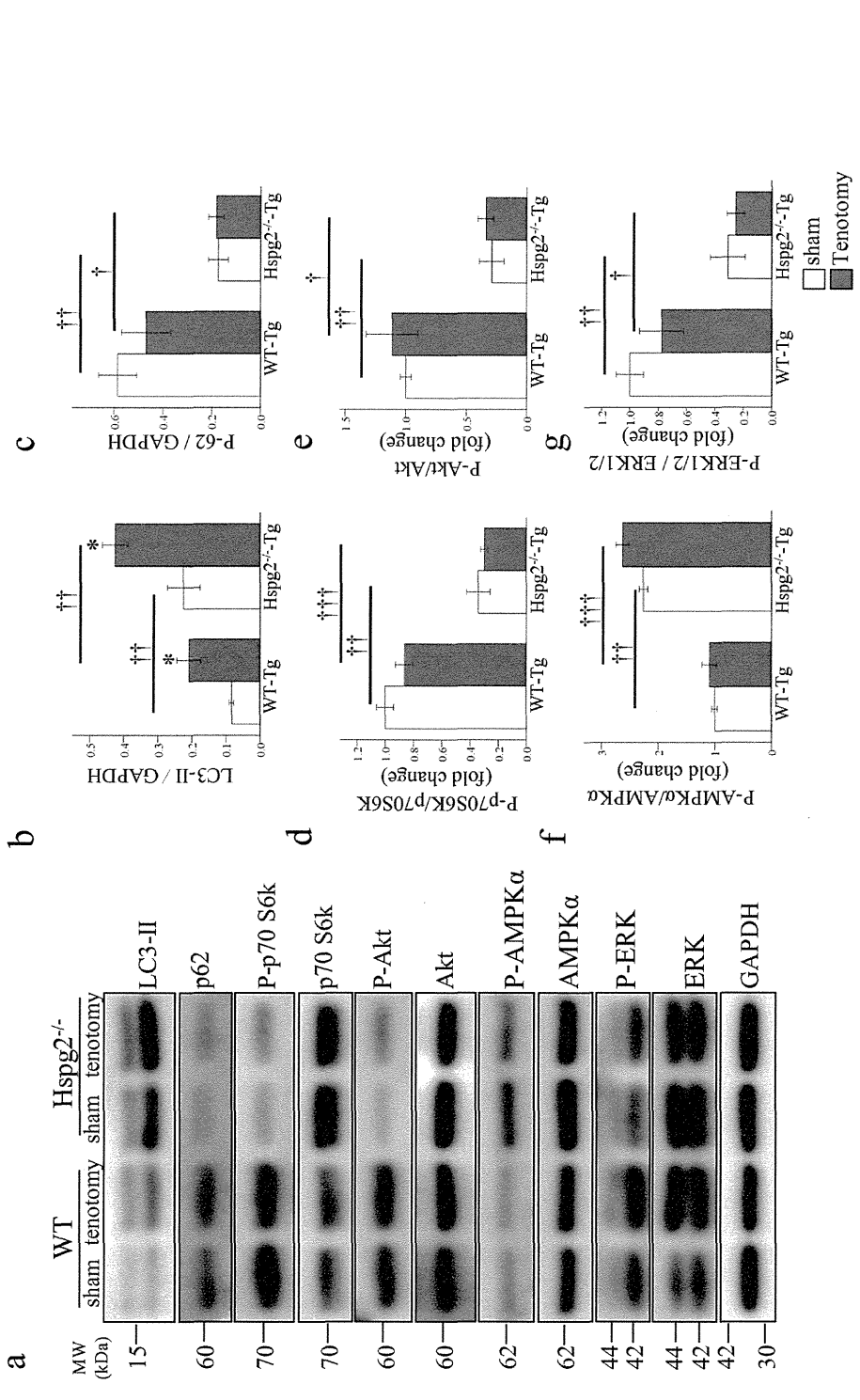

Fig. 5. Activity of the Akt/mTORC1 pathway in the sham and tenotomized soleus muscles from WT-Tg and Hspg2$^{-/-}$ Tg mice. (a) Immunoblotting results represent the levels of LC3II, p62, P-p70S6K, P-Akt, P-AMPKα, P-ERK in the sham and tenotomized soleus muscles from WT-Tg and Hspg2$^{-/-}$Tg mice. (b) Densitometric quantification of LC3II and p62 levels, normalized against GAPDH. Each value represents the mean ± s.e.m. $^{\dagger}P < 0.05$, $^{\dagger\dagger}P < 0.01$ vs. WT-Tg mice. (d, e, f, g) Relative activity, expressed as the ratio of activated phosphor-p70S6K to total p70S6K, phospho-Akt to total Akt, phosphor-AMPKα to total AMPKα and phospho-ERK to total ERK, was quantified as the fold increase relative to sham soleus muscles of WT-Tg mice. Each value represents the mean ± s.e.m. $^{\dagger}P < 0.05$; $^{\dagger\dagger}P < 0.01$; $^{\dagger\dagger\dagger}P < 0.001$ vs. WT-Tg mice.

Please cite this article as: L. Ning, et al., Perlecan inhibits autophagy to maintain muscle homeostasis in mouse soleus muscle, Matrix Biol (2015), http://dx.doi.org/10.1016/j.matbio.2015.08.002

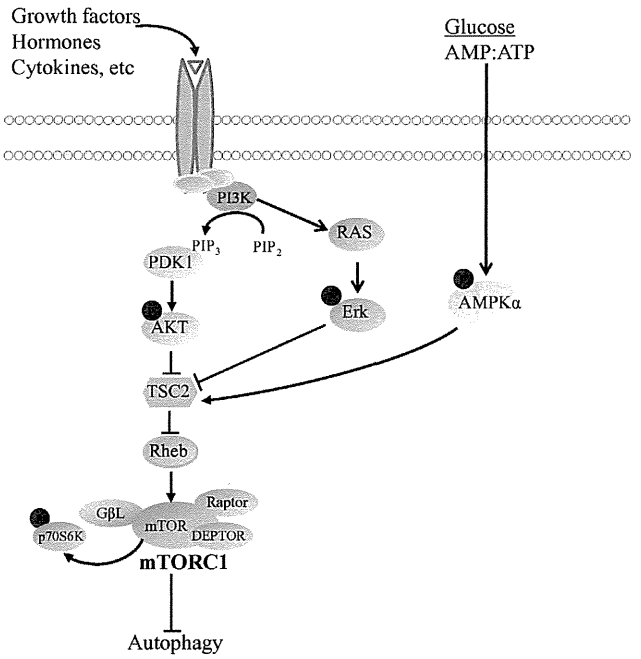

Fig. 6. Schematic representation of the mTORC1 signaling pathway. Autophagy is negatively regulated by mTOR via the formation of mTORC1. Akt functions as an upstream activator of the mechanistic target of mTORC1. mTORC1 phosphorylates its downstream targets p70 ribosome S6 kinase (p70S6K). Low glucose activates AMPKα, which directly phosphorylates the TCS2 tumor suppressor and leads to the inactivation of mTORC1 kinase. Erk1/2 can be activated by insulin-like growth factor 1 (IGF1) and inhibits the TSC1/TSC2 complex, activating mTORC1.

Perlecan deficiency increases basal autophagic activity through the inhibition of the mTORC1 pathway

Because the autophagy seemed to be overactive in Hspg2$^{-/-}$Tg soleus muscles, we further confirmed the basal autophagic activity and explored the ability of 15-week-old WT-Tg and Hspg2$^{-/-}$Tg mice to increase autophagy flux in the soleus muscle when submitted to a physiological stimulus such as fasting [28]. In order to differentiate between basal and starvation-induced autophagy, mice were examined under refed and starved conditions. Refed mice were fasted for 24 h and then refed for 2 h. The level of the lipidated form of microtubule-associated protein-1 light chain 3 (LC3-II), which is generated during autophagosome formation and reflects active autophagy [29], was significantly higher both in the refed and starved soleus from the Hspg2$^{-/-}$Tg mice as compared with those of the WT-Tg mice. However, the level of p62, a protein known to be incorporated into autophagosomes and efficiently degraded [30], was decreased (Fig. 4a–c). The mammalian target of rapamycin kinase complex 1 (mTORC1) is a critical regulator of autophagy induction, with activated mTORC1 suppressing autophagy, and the negative regulation of mTORC1 promoting it [31]. p70S6K is the main mTORC1 substrate regarded as an mTORC1 activation marker [32]. In WT-Tg mice, autophagy was induced under starved conditions, as shown by the increased level of LC3-II and the decreased level of p62 as compared with refed mice (Figs. 4a-c). This induction of autophagy correlated with mTORC1/p70S6K inhibition (Fig. 4a and d). In Hspg2$^{-/-}$Tg mice, autophagy was also induced under starved conditions (Fig. 4a-c). However, in contrast to WT-Tg mice, Hspg2$^{-/-}$Tg mice showed constant low levels of phosphorylation of p70S6K (Fig. 4a and d).

We analyzed the activation of Akt to determine if inhibition of the mTORC1 pathway in the absence of perlecan is associated with the Akt pathway, which functions as an upstream activator of the mechanistic target of mTORC1 and is a downstream target for mTORC2 [33], We found that perlecan deficiency decreased phosphorylation levels of Akt (Fig. 4a and e). Starved condition decreased the phosphorylation levels of Akt in WT-Tg mice but not in Hsp2$^{-/-}$Tg mice (Fig. 4a and e). We also investigated the activation of AMPKα to determine if the inhibition of the mTORC1 pathway in the absence of perlecan is associated with the AMPK pathway, which directly phosphorylates the TCS2 tumor suppressor and leads to the inactivation of mTORC1 kinase [34,35]. We found that perlecan deficiency enhanced phosphorylation levels of AMPKα and starved condition

Please cite this article as: L. Ning, et al., Perlecan inhibits autophagy to maintain muscle homeostasis in mouse soleus muscle, Matrix Biol (2015), http://dx.doi.org/10.1016/j.matbio.2015.08.002

promoted the phosphorylation levels of AMPKα in both WT-Tg and Hsp2$^{-/-}$Tg mice (Fig. 4a and f). To examine if the inhibition of the mTORC1 pathway in the absence of perlecan is growth factor-dependent, we investigated the activation of the ERK1/2 pathway, which can be activated by insulin-like growth factor 1 (IGF1) and inhibits the TSC1/TSC2 complex, activating mTORC1 [36]. The basal phosphorylation level of Erk1/2 was similar between Hspg2$^{-/-}$-Tg and WT-Tg mice. Starved condition induced a significant increase in the phosphorylation levels of Erk1/2 in the WT-Tg mice, whereas this effect was much less in Hspg2$^{-/-}$-Tg mice (Fig. 4g). These data suggests that perlecan deficiency activates the autophagy pathway via the mTORC1 pathway.

Mechanical unloading-induced autophagy is independent of the mTORC1 pathway in the soleus muscle

We have demonstrated that autophagic activity is increased in Hspg2$^{-/-}$Tg soleus muscle, which is associated with an increased atrophy rate. To investigate whether the mTORC1 pathway regulates unloading soleus muscle atrophy via the autophagy pathway, we tested the activity of the mTORC1 pathway in the unloading soleus muscles of WT-Tg and Hspg2$^{-/-}$Tg mice. We found that mechanical unloading increased LC3-II levels (Fig. 5a and b), but it did not change p62 levels in both the WT-Tg and Hspg2$^{-/-}$Tg mice (Fig. 5a, c). The phosphorylation level of p70S6K was significantly lower in both the sham and tenotomized soleus muscles of the Hspg2$^{-/-}$Tg mice as compared with those of the WT-Tg mice. However, the phosphorylation levels of p70S6k in the tenotomized muscles were similar to those of the sham muscles in both the WT-Tg and Hspg2$^{-/-}$ mice (Fig. 5a and d), indicating that mechanical unloading does not affect the activity of the mTORC1 pathway, regardless of the presence or absence of perlecan. Perlecan deficiency enhanced the phosphorylation levels of AMPKα and decreased the phosphorylation levels of Akt and ERK in Hsp2$^{-/-}$Tg mice. However, mechanical unloading did not affect the phosphorylation levels of AMPKα, Akt, and ERK in either the WT-Tg or the Hsp2$^{-/-}$Tg mice (Fig. 5a, f, g). Together with the data from the atrophy-deficient mouse model, these results demonstrate that tenotomy-induced autophagy is independent of the mTORC1 pathway in soleus muscles.

Discussion

Two major signaling pathways control skeletal muscle growth; the myostatin-Smad3 pathway acts as a negative regulator, and the insulin-like growth factor 1-phosphoinositide-3-kinase-Akt/protein kinase B-mammalian target of rapamycin (IGF1–PI3K–Akt/PKB–mTOR) pathway acts a positive regulator of muscle growth [37]. Our previous studies have shown that perlecan deficiency in fast-twitch muscles results in hypertrophy and decreased myostatin expression. Perlecan deficiency ameliorates atrophy in unloading fast-twitch muscles, but it fails to improve atrophy in unloading slow-twitch muscles [13]. This suggests that myostatin reduction induced by perlecan deficiency contributes to the improvement of atrophy in unloading fast-twitch muscles; however, because the slow-twitch muscle contains little myostatin, skeletal muscle atrophy cannot be inhibited. It has been shown that the Akt/mTORC1 signaling pathway negatively regulates the autophagy pathway (Fig. 6) [34,35]. In this study, we show that perlecan plays an important role in the maintenance of muscle mass by modulating autophagy. In our previous study, the absence of perlecan does not affect the level of muscle mass in the slow-twitch soleus muscles under unloading conditions [13]. However, in this study, our CSAs analyses revealed that perlecan deficiency affected unloading soleus muscle atrophy ($P < 0.01$). Also increased number of wet weights analyses showed the significant difference ($P < 0.04$) between control and perlecan deficient soleus muscle. These results suggest that perlecan is important to regulate mechanical stress in homeostasis of slow-twitch muscles.

Autophagy plays a pivotal role in skeletal muscle atrophy, which requires massive protein degradation [38]. It has been shown that soleus muscles from autophagy-impaired Atg7 KO mice maintain muscle mass after denervation [3]. A diverse collection of matrix constituents can modulate the autophagic signaling pathways [19]. In this study, we showed that the absence of perlecan in muscles increased the level of tenotomy-induced atrophy in the soleus muscle through the autophagy pathway. To the best of our knowledge, this report is the first to show the association between perlecan and autophagy. The present results suggest that perlecan inhibits the autophagic process via the mTORC1 signaling pathway in the mouse soleus muscle. In our previous study, we showed that FGF-2 mediated neurogenesis is impaired in the absence of perlecan, and that the activation of Akt, a major downstream signaling pathway of FGF-2, is also impaired in perlecan-deficient mice [12]. Thus, in this study, there was a possibility that the activation of Akt was also impaired in the soleus muscle in Hspg2$^{-/-}$Tg mice, resulting in the upregulation of the autophagy pathway; however, this remains to be directly investigated. The C-terminal fragment of perlecan, endorepellin, has been shown to promote autophagy in endothelial cells by regulating the expression of autophagy marker genes [23]. These results suggest

Please cite this article as: L. Ning, et al., Perlecan inhibits autophagy to maintain muscle homeostasis in mouse soleus muscle, Matrix Biol (2015), http://dx.doi.org/10.1016/j.matbio.2015.08.002

that the whole perlecan protein and its processed endorepellin molecule have distinct functional roles.

The present study demonstrates starvation-induced autophagic activity in both WT-Tg mice and Hspg2$^{-/-}$ Tg mice, but the unaltered mTORC1 pathway activity was not consistent with the induced autophagy observed in the Hspg2$^{-/-}$Tg mice. The explanation for this may be that perlecan deficiency induces constant low basal activity regarding the mTORC1 pathway and therefore that the activity of this pathway cannot be further reduced following the induction of autophagy. However, it was found that tenotomy did not change the phosphorylation level of p70S6K either in the WT-Tg or Hspg2$^{-/-}$Tg soleus muscles, suggesting that the tenotomy-induced activation of autophagy is independent of the mTORC1 signaling pathways. Muscle atrophy caused by immobilization [39] or unloading [40] is associated with oxidative stress. Therefore, it may be possible that the oxidative stress induced by tenotomy upregulates the autophagy signaling pathway via an mTORC1-independent pathway, but this has yet to be directly determined. In summary, our findings suggest that perlecan is a critical extracellular matrix component of skeletal muscle and serves to maintain soleus muscle mass and suppress the autophagic pathway via the activation of the mTORC1 pathway.

Materials and methods

Mice

Perlecan-deficient (Hspg2$^{-/-}$) mice die perinatally due to premature cartilage development [4,41]. To rescue cartilage abnormalities, we used a cartilage-specific Col2a1 promoter/enhancer to generate a perlecan transgenic mouse line (WT-Tg, Hspg2$^{+/+}$; Col2a1-Hspg2Tg/$^{-}$) that expressed recombinant perlecan in the cartilage [25]. We subsequently created lethality-rescued mice (Hspg2$^{-/-}$-Tg, Hspg2$^{-/-}$; Col2a1-Hspg2Tg/$^{-}$) by mating the transgenic mice with heterozygous Hspg2$^{+/-}$ mice [13]. We maintained these mice on a mixed genetic background of C57BL/6 and 129SvJ. In this study, WT-Tg mice (control) mice and Hspg2$^{-/-}$-Tg mice were used. GFP-LC3 (GFP-LC3-Tg) transgenic mice have been previously described [28]. Double transgenic Hspg2$^{-/-}$Tg and GFP-LC3-Tg mice were generated and used for the evaluation of GFP-LC3 puncta. Atg7 KO mice were described previously [3]. All animal protocols were approved by the Animal Care and Use Committee of Juntendo University.

Tenotomy procedures and tissue preparation

Tenotomies were performed under aseptic conditions under anesthesia. In each group of WT-Tg and Hsp2$^{-/-}$Tg mice, the right hindlimbs underwent sham surgeries (sham) and the left hindlimbs had the distal tendons of the gastrocnemius and soleus muscles tenotomized (G/S-Ten) [13]. Fourteen days after surgery, the hindlimb muscles were harvested, wet weighted, pinned on a cork, and immediately frozen in acetone cooled with dry ice. The muscles were stored at −80 °C for subsequent experiments.

Histochemistry

Muscles frozen in acetone were cross-sectioned (7 μm) mid-belly and fixed in 1.5% formalin. Sections were then stained with H&E following standard procedures [42]. The CSAs were analyzed using Image-Pro Plus software.

Fluorescence microscopy and electron microscopy

Cryosections of muscle transfected with GFP-LC3 were examined using a fluorescence microscope, and fluorescent dots were counted as described previously, normalizing for CSA [28]. For electron microscopy analysis, the muscles were directly fixed in 2.5% glutaraldehyde in 0.1 M cacodylate buffer on ice. Embedding and sectioning were performed by the Laboratory of Ultrastructural Research, Juntendo University. For statistical analysis, we studied at least 1000 muscle fibers. We considered positive fibers presenting at least one autophagic vesicle [20].

Western blot analyses

The mouse skeletal muscle extracts were prepared by homogenizing the tissues in a lysis buffer containing 50 mM Tris (pH 7.6), 0.5% sodium deoxycholate, 150 mM NaCl, 1 mM EDTA, 1% Triton X-100, protease, and phosphatase inhibitor cocktails (Complete Protease Inhibitor Cocktail and PhosSTOP; Roche, Rotkreuz, Switzerland). Samples were centrifuged at 12,000 × *g* for 15 min at 4 °C to collect the cytosolic fraction. The protein was quantified via BCA assay (Thermo Scientific, Rockford, IL) and subjected to Western blot analysis with anti-LC3A/B (1:1000; Cell Signaling, Danvers, MA, USA), anti-P62 (1:1000; Progen, Germany), anti-phospho-p70S6 kinase (1:1000; Cell Signaling), anti-phospho-Akt (1:1000; Cell Signaling), anti-Akt (1:1000; Cell Signaling), anti-p70S6 kinase (1:1000; Cell Signaling), anti-phospho-AMPKα (1:1000; Cell Signaling), anti-AMPKα (1:1000; Cell Signaling), anti-phospho-Erk1/2 (1:1000; Cell Signaling), anti-Erk1/2 (1:1000; Cell Signaling), and anti-GAPDH (1:500; Millipore, MA, USA) antibodies. Densitometric analysis was performed using Multi Gauge V3.0.

Please cite this article as: L. Ning, et al., Perlecan inhibits autophagy to maintain muscle homeostasis in mouse soleus muscle, Matrix Biol (2015), http://dx.doi.org/10.1016/j.matbio.2015.08.002

Statistical analysis

All values are expressed as mean ± SE. A two-sided Student's *t*-test was used for comparisons between the two groups. A P value < 0.05 was considered statistically significant. For all experiments, four mice/groups were used.

Author contributions

L. N. and E. A.-H. designed the project. L. N. performed the experiments, collected and analyzed the data, and prepared the manuscript. L. N. and Z. X. created tenotomized mouse models. N. F. helped conceive experiments and designed the overall study. R. N. performed the breeding and genotyping of mice. E. A.-H. contributed to the design and overall direction of the project. Y. Y. analyzed the data and provided suggestions. All authors contributed to the discussion and approved the final manuscript.

Competing financial interests

The authors declare no competing financial interests.

Acknowledgments

We wish to thank Andrew Cho and Ashok B. Kulkarni for their help in creating the mutant mice. This work was supported by grants from the Intramural Research Program of the NIDCR (DE000185-27 to YY), grants from the Japan Agency for Medical Research and Development (AMED, 15ek0109017s0202 to EAH), an Intramural Research Grant (26-8) for Neurological and Psychiatric Disorders of NCNP (EAH), and the MEXT-supported Program for the Strategic Research Foundation at Private Universities (S1101009 2011–2015).

Received 18 March 2015;
Received in revised form 19 August 2015;
Accepted 22 August 2015
Available online xxxx

Keywords:
Perlecan;
Muscle atrophy;
Autophagy;
Mechanical stress;
Soleus muscle

Current affiliation: Jilin University, China.

Abbreviations used:
ECM, extracellular matrix; Con, control; CSA, cross-sectional area; G/S-Ten, gastrocnemius and soleus muscles tenotomized; WT-Tg, wild type of perlecan alleles, containing Col2a1-perlecan transgene ($Hspg2^{+/+}$, Col2a1-Tg/+); $Hspg2^{-/-}$Tg, knockout perlecan alleles, containing Col2a1-perlecan transgene ($Hspg2^{-/-}$, Col2a1-Hspg2Tg/+).

References

[1] M.A. Ruegg, D.J. Glass, Molecular mechanisms and treatment options for muscle wasting diseases, Annu. Rev. Pharmacol. Toxicol. 51 (2011) 373–395.
[2] P. Bialek, C. Morris, J. Parkington, et al., Distinct protein degradation profiles are induced by different disuse models of skeletal muscle atrophy, Physiol. Genomics 43 (2011) 1075–1086.
[3] N. Furuya, S.I. Ikeda, S. Sato, et al., PARK2/parkin-mediated mitochondrial clearance contributes to proteasome activation during slow-twitch muscle atrophy via NFE2L1 nuclear translocation, Autophagy 10 (2014).
[4] E. Arikawa-Hirasawa, H. Watanabe, H. Takami, et al., Perlecan is essential for cartilage and cephalic development, Nat. Genet. 23 (1999) 354–358.
[5] E. Arikawa-Hirasawa, Y. Yamada, Roles of perlecan in development and disease: studies in knockout mice and human disorders, Seikagaku J. Jpn. Biochem. Soc. 73 (2001) 1257–1261.
[6] E. Arikawa-Hirasawa, S.G. Rossi, R.L. Rotundo, et al., Absence of acetylcholinesterase at the neuromuscular junctions of perlecan-null mice, Nat. Neurosci. 5 (2002) 119–123.
[7] R.V. Iozzo, L. Schaefer, Proteoglycan form and function: a comprehensive nomenclature of proteoglycans, Matrix Biol. 42 (2015) 11–55.
[8] R. Nonaka, T. Iesaki, S. de Vega, et al., Perlecan deficiency causes endothelial dysfunction by reducing the expression of endothelial nitric oxide synthase, Phys. Rep. 3 (2015).
[9] I.V. Fuki, R.V. Iozzo, K.J. Williams, Perlecan heparan sulfate proteoglycan: a novel receptor that mediates a distinct pathway for ligand catabolism, J Biol Chem 275 (2000) 25742–25750.
[10] M.S. Lord, C.Y. Chuang, J. Melrose, et al., The role of vascular-derived perlecan in modulating cell adhesion, proliferation and growth factor signaling, Matrix Biol. 35 (2014) 112–122.
[11] L. Schaefer, Proteoglycans, key regulators of cell-matrix dynamics, Matrix Biol. 35 (2014) 1–2.
[12] A. Kerever, F. Mercier, R. Nonaka, et al., Perlecan is required for FGF-2 signaling in the neural stem cell niche, Stem Cell Res. 12 (2014) 492–505.
[13] Z. Xu, N. Ichikawa, K. Kosaki, et al., Perlecan deficiency causes muscle hypertrophy, a decrease in myostatin expression, and changes in muscle fiber composition, Matrix Biol. 29 (2010) 461–470.
[14] C.J. Carlson, F.W. Booth, S.E. Gordon, Skeletal muscle myostatin mRNA expression is fiber-type specific and increases during hindlimb unloading, Am. J. Physiol 277 (1999) R601–R606.
[15] N.Y. Lin, C. Beyer, A. Giessl, et al., Autophagy regulates TNFalpha-mediated joint destruction in experimental arthritis, Ann. Rheum. Dis. 72 (2013) 761–768.

Please cite this article as: L. Ning, et al., Perlecan inhibits autophagy to maintain muscle homeostasis in mouse soleus muscle, Matrix Biol (2015), http://dx.doi.org/10.1016/j.matbio.2015.08.002

[16] A.M. Choi, S.W. Ryter, B. Levine, Autophagy in human health and disease, N. Engl. J. Med. 368 (2013) 1845–1846.
[17] N. Mizushima, T. Yoshimori, B. Levine, Methods in mammalian autophagy research, Cell 140 (2010) 313–326.
[18] D.C. Rubinsztein, P. Codogno, B. Levine, Autophagy modulation as a potential therapeutic target for diverse diseases, Nat. Rev. Drug Discov. 11 (2012) 709–730.
[19] T. Neill, L. Schaefer, R.V. Iozzo, Instructive roles of extracellular matrix on autophagy, Am. J. Pathol. 184 (2014) 2146–2153.
[20] P. Grumati, L. Coletto, P. Sabatelli, et al., Autophagy is defective in collagen VI muscular dystrophies, and its reactivation rescues myofiber degeneration, Nat. Med. 16 (2010) 1313–1320.
[21] V. Carmignac, M. Svensson, Z. Korner, et al., Autophagy is increased in laminin alpha2 chain-deficient muscle and its inhibition improves muscle morphology in a mouse model of MDC1A, Hum. Mol. Genet. 20 (2011) 4891–4902.
[22] G. Bix, J. Fu, E.M. Gonzalez, et al., Endorepellin causes endothelial cell disassembly of actin cytoskeleton and focal adhesions through alpha2beta1 integrin, J Cell Biol. 166 (2004) 97–109.
[23] C. Poluzzi, J. Casulli, A. Goyal, et al., Endorepellin evokes autophagy in endothelial cells, J Biol Chem. 289 (2014) 16114–16128.
[24] M. Ishijima, N. Suzuki, K. Hozumi, et al., Perlecan modulates VEGF signaling and is essential for vascularization in endochondral bone formation, Matrix Biol. 31 (2012) 234–245.
[25] N. Tsumaki, K. Tanaka, E. Arikawa-Hirasawa, et al., Role of CDMP-1 in skeletal morphogenesis: promotion of mesenchymal cell recruitment and chondrocyte differentiation, Eur. J. Cell Biol. 144 (1999) 161–173.
[26] C. Mammucari, G. Milan, V. Romanello, et al., FoxO3 controls autophagy in skeletal muscle in vivo, Cell Metab. 6 (2007) 458–471.
[27] S.E. Wohlgemuth, A.Y. Seo, E. Marzetti, et al., Skeletal muscle autophagy and apoptosis during aging: effects of calorie restriction and life-long exercise, Exp. Gerontol. 45 (2010) 138–148.
[28] N. Mizushima, A. Yamamoto, M. Matsui, et al., In vivo analysis of autophagy in response to nutrient starvation using transgenic mice expressing a fluorescent autophagosome marker, Mol. Biol. Cell 15 (2004) 1101–1111.
[29] Y. Kabeya, N. Mizushima, T. Ueno, et al., LC3, a mammalian homologue of yeast Apg8p, is localized in autophagosome membranes after processing, EMBO J. 19 (2000) 5720–5728.
[30] M. Komatsu, S. Waguri, M. Koike, et al., Homeostatic levels of p62 control cytoplasmic inclusion body formation in autophagy-deficient mice, Cell 131 (2007) 1149–1163.
[31] S. Alers, A.S. Loffler, S. Wesselborg, et al., Role of AMPK–mTOR–Ulk1/2 in the regulation of autophagy: cross talk, shortcuts, and feedbacks, Mol. Cell. Biol. 32 (2012) 2–11.
[32] G.G. Chiang, R.T. Abraham, Phosphorylation of mammalian target of rapamycin (mTOR) at Ser-2448 is mediated by p70S6 kinase, J. Biol. Chem. 280 (2005) 25485–25490.
[33] A. Parrales, E. Lopez, I. Lee-Rivera, et al., ERK1/2-dependent activation of mTOR/mTORC1/p70S6K regulates thrombin-induced RPE cell proliferation, Cell. Signal. 25 (2013) 829–838.
[34] K. Inoki, Y. Li, T. Xu, et al., Rheb GTPase is a direct target of TSC2 GAP activity and regulates mTOR signaling, Genes Dev. 17 (2003) 1829–1834.
[35] K. Inoki, T. Zhu, K.L. Guan, TSC2 mediates cellular energy response to control cell growth and survival, Cell 115 (2003) 577–590.
[36] M.C. Mendoza, E.E. Er, J. Blenis, The Ras-ERK and PI3K–mTOR pathways: cross-talk and compensation, Trends Biochem. Sci. 36 (2011) 320–328.
[37] S. Schiaffino, K.A. Dyar, S. Ciciliot, et al., Mechanisms regulating skeletal muscle growth and atrophy, FEBS J. 280 (2013) 4294–4314.
[38] W.E. Mitch, A.L. Goldberg, Mechanisms of muscle wasting. The role of the ubiquitin–proteasome pathway, N. Engl. J. Med. 335 (1996) 1897–1905.
[39] H. Kondo, M. Miura, Y. Itokawa, Oxidative stress in skeletal muscle atrophied by immobilization, Acta Physiol. Scand. 142 (1991) 527–528.
[40] J.M. Lawler, W. Song, S.R. Demaree, Hindlimb unloading increases oxidative stress and disrupts antioxidant capacity in skeletal muscle, Free Radic. Biol. Med. 35 (2003) 9–16.
[41] M. Costell, E. Gustafsson, A. Aszodi, et al., Perlecan maintains the integrity of cartilage and some basement membranes, J Cell Biol. 147 (1999) 1109–1122.
[42] C. Sciorati, B.G. Galvez, S. Brunelli, et al., Ex vivo treatment with nitric oxide increases mesoangioblast therapeutic efficacy in muscular dystrophy, J. Cell Sci. 119 (2006) 5114–5123.

Please cite this article as: L. Ning, et al., Perlecan inhibits autophagy to maintain muscle homeostasis in mouse soleus muscle, Matrix Biol (2015), http://dx.doi.org/10.1016/j.matbio.2015.08.002

Magn Reson Med Sci

TECHNICAL NOTE

E-pub ahead of print by J-STAGE
doi:10.2463/mrms.2014-0142

See-through Brains and Diffusion Tensor MRI Clarified Fiber Connections: A Preliminary Microstructural Study in a Mouse with Callosal Agenesis

Aurelien KEREVER[1], Koji KAMAGATA[2]*, Suguru YOKOSAWA[3], Yosuke OTAKE[3], Hisaaki OCHI[3], Taihei YAMADA[1], Masaaki HORI[2], Kouhei KAMIYA[4], Akira NISHIKORI[5], Shigeki AOKI[2], and Eri ARIKAWA-HIRASAWA[1]

[1]*Research Institute for Diseases of Old Age, Juntendo University Graduate School of Medicine 2–1–1 Hongo, Bunkyo-ku, Tokyo 113–8421, Japan*
[2]*Department of Radiology, Juntendo University Graduate School of Medicine*
[3]*Central Research Laboratory, Hitachi, Ltd.*
[4]*Department of Radiology, Graduate School of Medicine, The University of Tokyo*
[5]*Department of Radiological Sciences, Graduate School of Human Health Sciences, Tokyo Metropolitan University*

(Received December 8, 2014; Accepted January 28, 2015; published online March 31, 2015)

Clearing methods that render the brain optically transparent allow high-resolution three-dimensional (3D) imaging of neural networks. We used diffusion tensor imaging (DTI) and two-photon imaging of cleared brains to analyze white matter in BTBR mice. We confirmed corpus callosum agenesis and identified an abnormal commissure close to the third ventricle. DTI and cleared-brain two-photon imaging revealed that these commissural fibers constituted a frontal clustering of the ventral hippocampal commissure and provided a detailed assessment of white matter structure in mice.

Keywords: ***CLARITY, cleared brain, CUBIC, diffusion tensor imaging, mice***

Introduction

Various methods of rendering the mouse brain transparent (SCALEA2, CLARITY, SeeDB, 3DISCO, CUBIC) have recently been developed.[1,2] These techniques yield optical transparency and thus allow the creation of three-dimensional (3D) neural network images with single-cell resolution; they are therefore highly advantageous in neuroscience because they create novel perspectives completely different from those available with standard glass slide immunostaining. In addition, clinically oriented human brain imaging methods such as diffusion tensor imaging (DTI) have been applied to laboratory animals, enabling improvements in current experimental neuroscience. DTI allows researchers to measure the characteristics of local microstructural water diffusion in the brain,[3,4] taking advantage of the macroscopic geometric arrangement of white matter bundles.

*Corresponding author, Phone: +81-3-3813-3111, Fax: +81-3-5684-0476, E-mail: kkamagat@juntendo.ac.jp

The inbred BTBR T+tf/J (BTBR) mouse strain is a mouse model of autism that displays robust analogies to the diagnostic signs of this disorder in humans.[5] Neuroanatomical studies of the BTBR mouse brain have shown total agenesis of corpus callosum (CC) connective tissues, lack of a hippocampal commissure, and a putative accessory interhemispheric white matter tract that is implicated in abnormal behaviors.[6–8] Here, to better characterize the inter-hemispheric commissure in the BTBR strain of mice, we performed a neuroanatomical analysis by using both 3D high-resolution two-photon images of the transparent mouse brain and DTI. To our knowledge, this is the first report on the use of this dual procedure in the mouse brain.

Materials and Methods

Sample preparation

We performed two-photon analysis on the brains of five BTBR mice and five C57BL/6J (B6) mice (obtained from Jackson Laboratory, Bar Harbor, ME, USA) as controls. The brains of two of the

BTBR mice and two of the B6 mice were also scanned by MRI. Twelve-week-old male BTBR and B6 mice were deeply anesthetized and then perfused with 25 ml of ice-cold PBS-heparin (10 U/ml) solution followed by 25 ml of ice-cold paraformaldehyde (PFA) hydrogel solution (acrylamide 4%, bis 0.05%, Bio-Rad Laboratories, Inc., Hercules, CA, USA; PFA 4%, VA-044 initiator 0.25%, 145-05605, Wako Pure Chemical Industries Ltd., Osaka, Japan). The brain was carefully dissected and incubated in 10 ml of fresh hydrogel PFA solution in a sealed 50-ml conical tube for 2 days at 4°C. The tube containing the brain sample was then degassed and placed in a water bath for 3 h at 37°C for hydrogel polymerization. The brain was then carefully removed from the polymerized hydrogel and embedded in 1% agarose for MRI. All animal protocols were approved by the Animal Care and Use Committee of Juntendo University.

MRI

MR images were acquired within 2 weeks from perfusion using a 7T animal MRI system (MRI System, Agilent Technologies Inc., Palo Alto, CA, USA). The DTI sequence used was a 3D diffusion-weighted FSE, with TR = 300 ms, echo train length = 4, TE = 31.86 ms, two averages, field of view 19.2 × 19.2 × 19.2 mm, and matrix size 128 × 128 × 128, yielding an image with 150-μm isotropic voxels. The b value was 1,000 s/mm^2 (δ = 8 ms, Δ = 13.0 ms), and there were 30 diffusion directions. The total imaging time was 21 h and 10 min. Maps of fractional anisotropy (FA) and mean diffusivity (MD) were computed by using dTV II and VOLUMEONE 1.72, developed by Masutani et al.[9] Diffusion tensor tractography (DTT) of the BTBR mice and the B6 controls was performed with a deterministic fiber assignment by using a continuous tracking approach.[10] The FA threshold for tracking was set at 0.13, and the stop length was set at 160 steps. The bending angle of the tract was not allowed to exceed 45°.

In the B6 mice, we identified the corpus callosum (CC), dorsal hippocampal commissure (DHC), anterior commissure (AC), posterior commissure (PC), and ventral hippocampal commissure (VHC) as red areas on a mid-sagittal color-coded map (Fig. 1A). In BTBR mice, on the same type of map, we confirmed a total lack of the CC and DHC, although the AC and PC were present (Fig. 1E). We did not identify the VHC in BTBR mice, but we did find a red area in the rostral region of the third ventricle (Fig. 1E). The seed region of interest (ROI), including the entirety of the AC (blue), PC (yellow), and VHC (red) or abnormal commissure in the rostral region of the third ventricle (red), was placed manually on a reconstructed mid-sagittal isotropic diffusion-weighted image by referring to the mid-sagittal color-coded map (Fig. 1A, B, E, F). Because the habenular commissure (HBC) was a very small structure, we did not identify it in red on the mid-sagittal color-coded map; instead, we drew the seed ROI of the HBC on the mid-sagittal isotropic diffusion-weighted image while referring to a coronal non-diffusion-weighted image (Fig. 1C, G).

Tissue clearing and two-photon image acquisition

We used a modified version of the CLARITY[1] and CUBIC[2] protocols. The brain was removed from the agarose and washed in PBS-Triton X-100 (0.1%) for 1 h on a moving plate at 37°C. Sections (2 mm thick; coronal or sagittal) were obtained by using a mouse brain matrix (Muromachi Kikai Co., Ltd., Japan). Brain slices were incubated for 3 days at 37°C on a moving plate in a solution composed of 5 wt% urea (35904-45; Nacalai Tesque Inc., Japan), 25 wt% *N,N,N′,N′*-tetrakis(2-hydroxypropyl) ethylenediamine (T0781; Tokyo Chemical Industry Co., Ltd., Japan), and 15 wt% Triton X-100 (25987-85; Nacalai Tesque Inc.). The brain slices were washed in PBS-Triton X-100 (0.1%) overnight and then incubated with FluoroMyelin green (1:100; Invitrogen) for 5 days at 37°C on a moving plate. They were then washed in PBS-Triton X-100 (0.1%) overnight and incubated with a solution composed of 50 wt% sucrose (30403-55; Nacalai Tesque Inc.), 25 wt% urea, 10 wt% 2,20,20′-nitrilotriethanol (145-05605; Wako Pure Chemical Industries Ltd., Japan), and 0.1% (v/v) Triton X-100. Image acquisition was performed with a Carl Zeiss LSM 780 two-photon microscope (two-photon Chameleon laser; wavelength 800 nm) with a ×10 Plan Apochromat objective (numerical aperture 0.45; working distance 2 mm). Image processing was performed with Imaris Interactive Microscopy Image Analysis software (Bitplane).

Results

DTI and DTT revealed agenesis of the CC but intact inter-hemispheric tracts in the AC, PC, and HBC of all BTBR mice (Fig. 1), along with abnormal commissure fibers in the rostral region of the third ventricle. DTT revealed that these abnormal commissural fibers seemed to connect with the fimbria (Figs. 1H and 2B), which is the route followed by hippocampal axons to reach the hippocampal commissure at the midline. Therefore, we suspected that the abnormal inter-hemispheric commissure

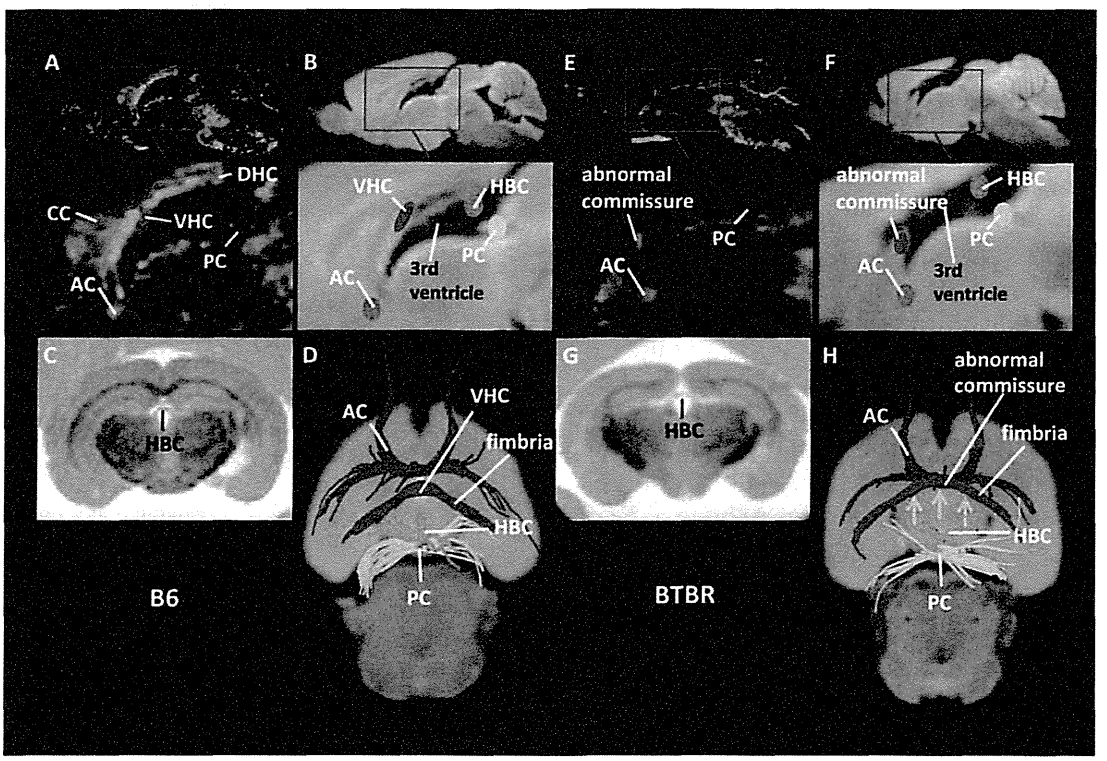

Fig. 1. Diffusion tensor imaging (DTI) and diffusion tensor tractography (DTT) of B6 mice and BTBR mice. Mid-sagittal color-coded fractional anisotropy (FA) map (**A**), isotropic diffusion-weighted image (**B**), coronal non-diffusion-weighted image (**C**), and DTT (**D**) in a B6 mouse. Mid-sagittal color-coded FA map (**E**), isotropic diffusion-weighted image (**F**), coronal non-diffusion-weighted image (**G**), and DTT (**H**) in a BTBR mouse.

was the VHC positioned more rostral than in B6 mice (Fig. 1D). By using two-photon imaging of cleared mouse brains, we assessed whether the abnormal commissural fibers were in fact connected to the fimbria. In all BTBR mice, they were indeed connected to it (Fig. 2A).

Discussion

There were two main findings of our analysis. First, in BTBR mice, we confirmed agenesis of the CC and found intact inter-hemispheric tracts in the AC, PC, and HBC. Second, we identified an abnormal inter-hemispheric commissure in the rostral region of the third ventricle, and we found that this abnormal commissure constituted a frontal clustering of the VHC.

The CC agenesis and intact inter-hemispheric tracts in the AC, PC, and HBC in BTBR mice were in line with the findings of previous reports.[6–8] In addition, Miller et al.[6] reported that the abnormal inter-hemispheric commissural fibers in the rostral region of the third ventricle constituted a novel connective inter-hemispheric structure between the left and right hemispheres that may contribute

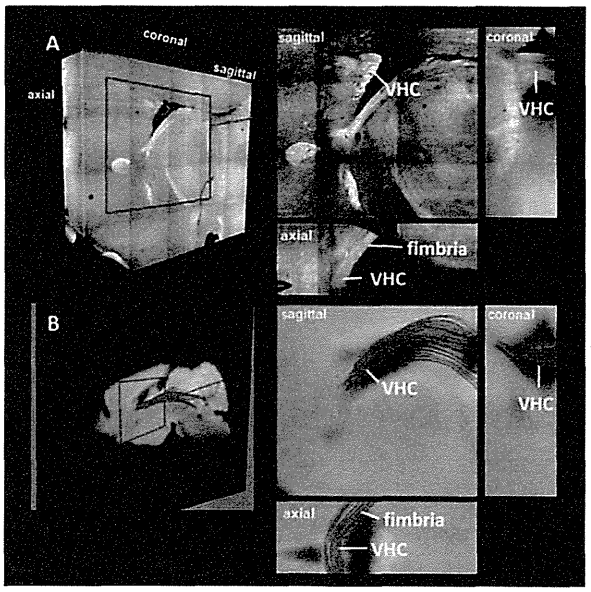

Fig. 2. Two-photon imaging of cleared BTBR mouse brain (**A**) and diffusion tensor tractography of BTBR mouse brain (**B**). In BTBR mice, the abnormal inter-hemispheric commissural fibers were connected to the fimbria; we considered them equivalent to the ventral hippocampal commissure (VHC).

to the behavioral abnormalities of BTBR mice. However, we confirmed by DTI and two-photon imaging that the abnormal inter-hemispheric commissural fibers in the rostral region of the third ventricle were connected to the fimbria. Wyss et al.[11] reported that the topographic organization of the fibers in the fimbria is reflected in the arrangement of the crossed components in the VHC. Therefore, the inter-hemispheric commissural fibers in the rostral region of the third ventricle in BTBR mice represent not a novel inter-hemispheric commissure, as reported by Miller et al.,[6] but the VHC.

White matter voxels in the brain contain multiple fiber bundles in tracts that are oriented in different directions (e.g., crossing, "kissing," and "fanning"); in these areas, DTT is not reliable.[12] DTT evaluations of the connectivity of nerve fibers can depict nerve fiber connectivity where none is present. By using 3D images of cleared mouse brains with single-cell resolution, we confirmed here that the inter-hemispheric fibers were connected to the fimbria. Because two-photon imaging of cleared mouse brains enables the evaluation of the brain microstructure with high resolution, it is useful for local-area characterization of the brain. However, evaluating macroscopic nerve fiber connectivity by this method is difficult. Therefore, combining DTI and two-photon imaging of cleared mouse brains improves the reliability of analyses of brain white matter connections.

Conclusion

DTI combined with two-photon imaging of the cleared mouse brains enables detailed assessment of white matter structure.

Acknowledgements

This work was supported by grants from MEXT-Supported Program for the Strategic Research Foundation at Private Universities (2011–2015) and a research grant from Hitachi, Ltd.

References

1. Chung K, Wallace J, Kim SY, et al. Structural and molecular interrogation of intact biological systems. Nature 2013; 497:332–337.
2. Susaki EA, Tainaka K, Perrin D, et al. Whole-brain imaging with single-cell resolution using chemical cocktails and computational analysis. Cell 2014; 157:726–739.
3. Basser PJ, Mattiello J, LeBihan D. Estimation of the effective self-diffusion tensor from the NMR spin echo. J Magn Reson B 1994; 103:247–254.
4. Kamagata K, Shimoji K, Hori M, et al Intersite reliability of diffusion tensor imaging on two 3T scanners. Magn Reson Med Sci 2015 Feb 12. [Epub ahead of print]
5. Scattoni ML, Ricceri L, Crawley JN. Unusual repertoire of vocalizations in adult BTBR T+tf/J mice during three types of social encounters. Genes Brain Behav 2011; 10:44–56.
6. Miller VM, Gupta D, Neu N, Cotroneo A, Boulay CB, Seegal RF. Novel inter-hemispheric white matter connectivity in the BTBR mouse model of autism. Brain Res 2013; 1513:26–33.
7. Wahlsten D, Metten P, Crabbe JC. Survey of 21 inbred mouse strains in two laboratories reveals that BTBR T/+ tf/tf has severely reduced hippocampal commissure and absent corpus callosum. Brain Res 2003; 971:47–54.
8. Dodero L, Damiano M, Galbusera A, et al. Neuroimaging evidence of major morpho-anatomical and functional abnormalities in the BTBR T+TF/J mouse model of autism. PLoS One 2013; 8:e76655.
9. Masutani Y, Aoki S, Abe O, Hayashi N, Otomo K. MR diffusion tensor imaging: recent advance and new techniques for diffusion tensor visualization. Eur J Radiol 2003; 46:53–66.
10. Mori S, Crain BJ, Chacko VP, van Zijl PC. Three-dimensional tracking of axonal projections in the brain by magnetic resonance imaging. Ann Neurol 1999; 45:265–269.
11. Wyss JM, Swanson LW, Cowan WM. The organization of the fimbria, dorsal fornix and ventral hippocampal commissure in the rat. Anat Embryol (Berl) 1980; 158:303–316.
12. Wiegell MR, Larsson HB, Wedeen VJ. Fiber crossing in human brain depicted with diffusion tensor MR imaging. Radiology 2000; 217:897–903.

Perlecan deficiency causes endothelial dysfunction by reducing the expression of endothelial nitric oxide synthase

ARTICLE · JANUARY 2015

DOI: 10.14814/phy2.12272

7 AUTHORS, INCLUDING:

Risa Nonaka
Juntendo University
11 PUBLICATIONS **96** CITATIONS
SEE PROFILE

Susana De Vega
Juntendo University
21 PUBLICATIONS **327** CITATIONS
SEE PROFILE

Takako Sasaki
Oita University
179 PUBLICATIONS **7,504** CITATIONS
SEE PROFILE

Eri Arikawa- Hirasawa
Juntendo University
75 PUBLICATIONS **1,758** CITATIONS
SEE PROFILE

Physiological Reports

Open Access

Physiological Reports ISSN 2051-817X

ORIGINAL RESEARCH

Perlecan deficiency causes endothelial dysfunction by reducing the expression of endothelial nitric oxide synthase

Risa Nonaka[1], Takafumi Iesaki[2], Susana de Vega[1], Hiroyuki Daida[3], Takao Okada[2], Takako Sasaki[4] & Eri Arikawa-Hirasawa[1]

1 Research Institute for Disease of Old Age, Juntendo University Graduate School of Medicine, Tokyo, Japan
2 Department of Physiology, Juntendo University Graduate School of Medicine, Tokyo, Japan
3 Department of Cardiovascular Medicine, Juntendo University Graduate School of Medicine, Tokyo, Japan
4 Department of Biochemistry, Faculty of Medicine, Oita University, Oita, Japan

Keywords
Endothelial cell, nitric oxide synthase, perlecan.

Correspondence
Eri Arikawa-Hirasawa, Juntendo University Graduate School of Medicine, Research Institute for Diseases of Old Age, 2-1-1 Hongo, Bunkyo-ku, Tokyo 113-8421, Japan.
Tel: +81-3-3814-3016
Fax: +81-3-3814-3016
E-mail: ehirasaw@juntendo.ac.jp

Funding Information
This work was supported by a Grant-in-Aid for Young Scientists (B) (24790783) to R.N. and a Grants-in-Aids from the Ministry of Education, Culture, Sports, Science and Technology as well as the Ministry of Health, Labor and Welfare of Japan, Grant for Neurological and Psychiatric Disorders of NCNP (26-8) to E A-H. This study was supported by Grants from MEXT-Supported Program for the Strategic Research Foundation at Private Universities (2011–2015).

Received: 8 October 2014; Revised: 16 December 2014; Accepted: 17 December 2014

doi: 10.14814/phy2.12272

Physiol Rep, 3 (1), 2015, e12272, doi: 10.14814/phy2.12272

Risa Nonaka and Takafumi Iesaki have contributed equally to this work.

Abstract

Perlecan is a major heparan sulfate proteoglycan found in the subendothelial extracellular matrix of the vascular wall. The aim of this study was to investigate the role of perlecan in the regulation of vascular tone. A previously developed conditional perlecan-deficient mouse model was used to measure changes in the isometric force of isolated aortic rings. The vessels were first precontracted with phenylephrine, and then treated with increasing concentrations of vasorelaxants. Endothelium-dependent relaxation, elicited by acetylcholine, was significantly reduced in the perlecan-deficient aortas, whereas endothelium-independent relaxation caused by the exogenous nitric oxide donor sodium nitroprusside remained well preserved. The expression of the endothelial nitric oxide synthase (eNOS) gene, detected by real-time polymerase chain reaction, was significantly decreased in the perlecan-deficient aortas. The expression of eNOS protein detected using Western blotting was also significantly decreased in the perlecan-deficient aortas. We examined the role of perlecan in eNOS gene expression by creating perlecan knockdown human aortic endothelial cells using small interfering RNA (siRNA) for perlecan. Perlecan gene expression was significantly reduced in the perlecan siRNA-treated cells, resulting in a significant decrease in eNOS gene expression. Perlecan deficiency induced endothelial dysfunction, as indicated by a reduction in endothelium-dependent relaxation due, at least partly, to a reduction in eNOS expression. These findings suggest that perlecan plays a role in the activation of eNOS gene expression during normal growth processes.

Introduction

Vascular endothelial cells and vascular smooth muscle cells are two major research targets in the field of vascular physiology. The extracellular matrix in the vascular wall has recently attracted attention, as it not only provides structural support, but also modulates several cellular functions, including cellular adhesion, proliferation,

differentiation, and development (Pillarisetti 2000; Jiang and Couchman 2003; Iozzo 2005). The basement membrane is a thin sheet of the extracellular matrix that underlies the vascular endothelium and surrounds smooth muscle cells. Some of the key constituents of the subendothelial extracellular matrix are heparan sulfate proteoglycans (HSPGs). Perlecan (HSPG2) is a major HSPG in the basement membrane, with a molecular weight of over 400 kDa and a protein core consisting of five domains. It interacts with a number of extracellular matrix molecules, including laminin, collagen IV, fibronectin, fibrillin, and several growth factors, such as vascular endothelial growth factor (VEGF), fibroblast growth factors (FGFs), and platelet-derived growth factor (PDGF) (Iozzo 2005). Perlecan also interacts with plasma lipoprotein very low density lipoprotein (VLDL) (Hummel et al. 2004) and integrin cell surface receptor (Hummel et al. 2004). It also plays a role in a number of processes in the vasculature, including atherosclerosis, tumor angiogenesis, smooth muscle cell activity modulation, endothelial proliferation, and vascular development (Segev et al. 2004).

Others and we have previously reported that the homozygous deletion of *HSPG2* ($HSPG2^{-/-}$) in mice results in lethal chondrodysplasia and in cardiovascular abnormalities, such as transposition of the great arteries (Arikawa-Hirasawa et al. 1999; Costell et al. 1999, 2002). Perlecan deficiency ($HSPG2^{-/-}$) also causes perinatal lethal chondrodysplasia in humans (Costell et al. 1999; Arikawa-Hirasawa et al. 2001), suggesting a crucial role for perlecan in the development of cartilage and in the cardiovascular system. Mutations in the perlecan gene (*HSPG2*) have been identified in patients with Schwartz–Jampel syndrome, a nonlethal condition characterized by myotonia and mild chondrodysplasia (Nicole et al. 2000; Arikawa-Hirasawa et al. 2002; Stum et al. 2006). We investigated the role of perlecan in adult organs using a lethality rescued perlecan-null mouse model expressing recombinant perlecan specifically in cartilage ($HSPG2^{-/-}$-*Tg*) (Xu et al. 2010; Inomata et al. 2012; Ishijima et al. 2012; Kaneko et al. 2013). In addition to our lethality rescued $HSPG2^{-/-}$-*Tg* mouse model, studies employing mutant mice, such as heterozygous perlecan knockout ($HSPG2^{+/-}$) mice (Vikramadithyan et al. 2004) or heparan sulfate (HS)-deficient perlecan expressing mice (Tran-Lundmark et al. 2008), have provided further insights into the in vivo function of perlecan in adult tissues.

Endothelial dysfunction is considered to be a key variable in the pathogenesis of atherosclerosis and in its complications (Bonetti et al. 2002). The dysfunctional condition includes reduction in nitric oxide (NO) bioavailability, which may result in reduced vasorelaxation, thrombus formation, deposition of serum lipids, and the migration and proliferation of vascular smooth muscle cells (VSMCs), which leads to the formation of stenotic lesions in blood vessels (Cai and Harrison 2000). The regulation of vascular tone is the most widely studied aspect of the endothelial function, and NO is the major contributor to endothelium-dependent relaxation in large arteries. In the present study, we investigated the effects of perlecan deletion on endothelium-dependent vascular relaxation during the normal growth process and explored the mechanisms underlying the effects.

Materials and Methods

Animals

Perlecan-null ($HSPG2^{-/-}$) mice die perinatally due to premature cartilage development (Arikawa-Hirasawa et al. 1999; Costell et al. 1999). We previously created a perlecan transgenic mouse line (WT-Tg, $HSPG2^{+/+}$; *COL2A1-HSPG2*$^{Tg/-}$), which expresses recombinant perlecan in cartilage, using a cartilage-specific *COL2A1* promoter/enhancer (Tsumaki et al. 1999) to restore cartilage abnormalities. Subsequently, we created lethality-rescued mice ($HSPG2^{-/-}$ -Tg, $HSPG2^{-/-}$;*COL2A1-HSPG2*$^{Tg/-}$), by mating the transgenic mice with heterozygous $HSPG2^{+/-}$ mice (Xu et al. 2010). We maintained these mice on a mixed genetic background of C57BL/6 and 129SvJ. In the present study, we used $HSPG2^{-/-}$ -Tg mice for the experimental group and WT-Tg ($HSPG2^{+/+}$; *COL2A1-HSPG2*$^{Tg/-}$), mice (10 weeks of age) for the control group. All experimental procedures were performed in accordance with the guidelines for the care and use of animals at Juntendo University, Tokyo, Japan.

Measurement of changes in force in the mice aorta

The mice were sacrificed under anesthesia (Pentobarbital; 50 mg/kg, intraperitoneal administration). The descending thoracic aorta was isolated and cut into transverse rings (~2 mm in length), which were used to measure the changes in force. Care was taken not to touch the endothelial surface in order to preserve the functional endothelium. The techniques used to measure the changes in force were adapted from previously described methods (Iesaki et al. 1999; Sumiyoshi et al. 2008). Briefly, aortic rings were mounted on wire hooks attached to force displacement transducers (Nihon Kohden, Tokyo, Japan) and changes in the isometric force were recorded on a thermal recorder (Rika Denki, Tokyo, Japan). The rings were incubated in individually thermostated (37°C)

10-mL baths filled with oxygenated Krebs bicarbonate buffer (118 mmol/L NaCl, 4.7 mmol/L KCl, 1.5 mmol/L $CaCl_2$, 25 mmol/L $NaHCO_3$, 1.1 mmol/L $MgSO_4$, 1.2 mmol/L KH_2PO_4, and 5.6 mmol/L glucose at pH 7.4). An optimal passive tension of 0.5 g was applied to the rings throughout the experiment. The vascular rings were initially exposed to high-K^+ Krebs bicarbonate buffer, containing 60 mmol/L KCl in place of NaCl to produce maximal force and to enhance the reproducibility of subsequent contractions. After a wash out of high-K^+ buffer, the vessels were submaximally contracted with 1 μmol/L phenylephrine. Once a steady-state level of contraction was achieved, endothelial-dependent relaxation and endothelial-independent relaxation were elicited by the administration of increasing concentrations of acetylcholine (ACh) and sodium nitroprusside (SNP), respectively. Relaxation was expressed as the percent change in the steady-state level of contraction. Comparisons between groups were made with two-way reported measure ANOVA.

Quantitative real-time polymerase chain reaction

Total RNA was isolated from mouse thoracic aortic tissue or human aortic endothelial cells (HAECs; LONZA, Walkersville, MD) using TRIzol reagent (Life Technologies, Carlsbad, CA), according to the manufacturer's instructions. cDNA was generated from 1 μg of total RNA with M-MLV reverse transcriptase (Promega, Madison, WI) and a random primer (TAKARA, Siga, Japan). SYBR Green was used for detection, and RNA expression was normalized to that of the housekeeping gene β-actin for mouse, GAPDH for human. In the graph, the eNOS, von Willebrand factor, and perlecan (HSPG2) expression levels are indicated as relative to β-actin or GAPDH. The PCR reaction was carried out in an ABI Prism® 7500 Fast Sequence Detection System (Life Technologies). The primer sequences were as follows: For the mouse tissue, mouse eNOS forward 5′-CTGGCAGCCCAAGACCTA-3′, mouse eNOS reverse 5′-GTGACATCGCCGCAGACAA-3′, mouse von Willebrand factor forward 5′-GATGCCCCAGTCAGCTCTAC-3′, mouse von Willebrand factor reverse 5′- TCAGCCTCGGACAACATAGA-3′, mouse β-actin forward 5′-TGGAATC CTGTGGCATCCATGAAAC-3′, mouse β-actin reverse 5′-TAAAACGCAGCTCAGTAACAGTCCG-3′. For the HAECs, human HSPG2 forward 5′-GGCTGAGGGCATACGATGGCT-3′, human HSPG2 reverse 5′-CCCACTGC CCAGGTCGTCTCC-3′, human eNOS forward 5′-CCCTT CAGTGGCTGGTACAT-3′, human eNOS reverse 5′-CACGATGGTGACTTTGGCTA-3′, human GAPDH forward 5′-ACCACAGTCCATGCCATCAC-3′, human GAPDH reverse 5′-TCCACCACCCTGTTGCTGTA-3′

Western blotting

Thoracic aortic tissue was isolated and then homogenized in cold lysis buffer, and the lysate was centrifuged at 16,000 *g* for 15 min at 4°C. The lysis buffer contained 50 mmol/L Tris-HCl (pH 7.2), 150 mmol/L NaCl, 1% Nonidet P-40, 1% sodium deoxycholate, 0.1% SDS containing protease, and phosphatase inhibitor cocktails (Complete Protease Inhibitor Cocktail and PhosSTOP; Roche, Rotkreuz, Switzerland). The protein concentration was determined using a BCA protein assay kit (Thermo Scientific, Rockford, IL) and then solubilized in NuPAGE® LDS sample buffer (Life Technologies) containing dithiothreitol. The samples (15 μg/lane) were resolved via electrophoresis on 4–12% SDS-PAGE gels, and then transferred to a PVDF membrane (Life Technologies, Carlsbad, CA). After blocking with PVDF blocking reagent (TOYOBO, Osaka, Japan), the membrane was incubated with primary antibodies in blocking reagent overnight. After washing, the membrane was incubated with horseradish peroxidase (HRP)-conjugated secondary antibodies in blocking reagent and visualized with SuperSignal®West Dura Extended Duration Substrate (Thermo Scientific, Rockford, IL). Specific bands were quantitated using the ImageJ software program. In the graph, the eNOS protein level is indicated as relative to β-actin. The experiments were performed at least three times using different sibling pairs of animals. The antibodies were prepared as follows: the primary antibodies, mouse anti-eNOS/NOS type III antibodies (BD Biosciences, Franklin Lakes, NJ) or mouse anti-β-actin antibody (Santa Cruz Biotechnology, Inc., Dallas, TX) were diluted at 1:1000 or 1:5000 in blocking reagent. The secondary antibodies, anti-mouse IgG HRP-conjugated secondary antibodies (GE Healthcare, Little Chalfont, UK) were diluted at 1:5000 in blocking solution.

Cell culture and small interfering RNA (siRNA)

Human aortic endothelial cells (HAECs) were grown using the Endothelial Cell Growth Media Kit (EGM-2 BulletKit; LONZA), and plated at a density of 2×10^5 cells on 6-well plates. Perlecan siRNA and control siRNA were purchased from Santa Cruz Biotechnology. HAECs were transfected with either perlecan or control siRNA, according to the manufacturer's recommendations. Forty-eight hours after transfection, knockdown efficiency was assessed using quantitative RT-PCR (qPCR), as described above. For perlecan rescue experiments, we used the recombinant perlecan protein (rPerlecan) kindly provided by Dr. Sasaki. The recombinant perlecan was purified from the condition media of 293